JCTC Journal of Chemical Theory and Computation

pubs.acs.org/JCTC Article

PHAHST Potential: Modeling Sorption in a Dispersion-Dominated Environment

Logan Ritter,* Brant Tudor,* Adam Hogan, Tony Pham, and Brian Space*

Cite This: J. Chem. Theory Comput. 2024, 20, 5570−5582 Read Online

ACCESS | Metrics & More | Article Recommendations | Supporting Information

ABSTRACT: PHAHST (potentials with high accuracy, high speed, and transferability) is a recently developed force field that utilizes exponential repulsion, multiple dispersion terms, explicit many-body polarization, and many-body van der Waals interactions. The result is a systematic approach to force field development that is computationally practical. Here, PHAHST is employed in the simulation for rare gas uptake of krypton and xenon in the metal−organic material, HKUST-1. This material has shown promise in use as an adsorptive separating agent and presents a challenge to model due to the presence of heterogeneous interaction sorption surfaces, which include pores with readily accessible, open-metal sites that compete with dispersion-dominated pores. Such environments are difficult to simulate with commonly used empirical force fields, such as the Lennard-Jones (LJ) potential, which perform better when electrostatics are dominant in determining the nature of sorption and alone are incapable of modeling interactions with open-metal sites. The effectiveness of PHAHST is compared to the LJ potential in a series of mixed Kr−Xe gas simulations. It has been demonstrated that PHAHST compares favorably with experimental results, and the LJ potential is inadequate. Overall, we establish that force fields with physically grounded repulsion/dispersion terms are required in order to accurately model sorption, as these interactions are an important component of the energy. Furthermore, it is shown that the simple mixing rules work nearly quantitatively for the true pair potentials, while they are not transferable for effective potentials like LJ.

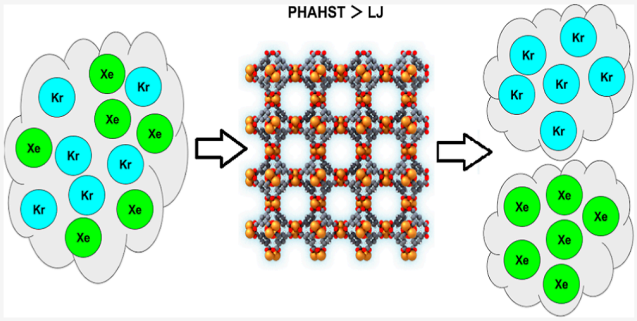

INTRODUCTION

The main goal of this paper is to explore the repulsion/dispersion properties of the newly developed PHAHST potential energy surface in a real-world system.[1−3] To put it simply, krypton and xenon are industrial gases used in a variety of processes, both of which are used in manufacturing light-generating products, ranging from lamps to lasers. Their separation is of particular importance in nuclear material processing and industrial applications.[4−8] Furthermore, these gases are a rarity in nature, and the process of obtaining them invariably requires a substantial energy investment.[9,10] A typical method of procurement is to separate these gases from the atmosphere, where they are found in trace amounts, a process involving multiple cryogenic distillations. The cost of these types separations is prohibitively expensive, accounting for nearly 15% of the world's total energy consumption in the case of hydrocarbon separation.[11] Low-cost and energy efficient methods for separating krypton from xenon are necessary for industry to have at its disposal. However, such separations are made difficult owing to the general similarity of xenon and krypton in terms of their physical properties. They pose a challenge to simulate for similar reasons; both gases have significant and similar dispersion and polarization interactions. These difficulties are compounded by the marked lack of chemical reactivity characteristic of noble gases. Accordingly, research groups have explored numerous possible methods of krypton/xenon separation in the search for a procedure that is both cost- and energy-efficient. A sample of the substitutes that have reported some level of success includes selective sorption by nanoporous metal formates,[12] sieving through zeolitic membranes,[13,14] chromatography via columns of activated carbon,[15] and selective adsorption by porous organic frameworks.[16,17] Recently, an emerging class of materials, metal−organic frameworks (MOFs), has been the focus of research efforts in this regard.

MOFs are a class of porous materials that are composed of organic linkers connected into regular, repeating crystalline 3D structures via metallic nodes. The length and shape of the linkers allow for pores and cavities of varying sizes, both of which can be rationally shaped and selected depending upon an application's

Received: February 22, 2024
Revised: May 30, 2024
Accepted: May 31, 2024
Published: June 18, 2024

requirements. Furthermore, the organic functional groups on the linkers can add specialized chemical functionality and can be engineered with intended purpose. The different coordination networks and topologies established by the metallic nodes, coupled with the vast quantity of suitable linker molecules, make for a large chemical space of possible MOFs. As a result, these materials have received a great deal of attention with use in a wide range of applications, such as gas storage,[18−20] catalysis,[21,22] and separations.[23,24] The potential for separating krypton from xenon via MOFs for these reasons has not escaped the attention of motivated researchers.[6,7,25−29]

The quantity of theoretically possible MOFs is vast, as are their behaviors and uses. As with most chemical explorations, the investment in terms of time, material, and financial resources required to synthesize prototypical MOFs can be significant. Additionally, the synthesis may require the use of hazardous chemicals. The resultant material, once realized, may still be found to underperform with regard to its expected behavior in the target application. Thus, reliable simulations can play an important role in guiding synthetic chemists in their search for useful materials. Some research groups have developed techniques for rapid examination of large quantities of MOFs, both known and hypothetical, and have proven effective at eliminating large swaths of materials from consideration while identifying potential targets that show exceptional promise for a given application.[25,30−33] Once the field has been narrowed to a few candidates, more robust simulations can be performed, which can give better predictions as to a material's behavior with regard to a specific function under a variety of conditions. Additionally, the detailed information available in a simulation can provide valuable insights as to which physical features (e.g., pore size, open-metal sites, and surface area) serve to enhance or attenuate properties of interest and to what extent. Data collected through experiment, likewise, aids computational efforts through providing information that is used to verify a model's accuracy or reveal its weak points. Each empirical data point represents an opportunity to increase the fidelity for future generations of model development, as the more accurately the system's energetics are captured in the potential model, the more valuable the insights that model can provide.

Often, sorbate/potential models are parametrized to fit bulk experimental data, such as liquid densities, heats, or free energies.[34−39] While matching experimental data is a reasonable approach in regards to accurately capturing bulk behavior, they cannot be expected to reproduce experimental data when the system involved contains molecular configurations or relative orientations, which are not widely represented in the bulk media. This includes configurations which often appear in heterogeneous environments or when polarization effects lead to otherwise unexplored conformations.[34,40,41] Furthermore, it has been shown that accounting for explicit polarization is often required for the accurate capture of sorbate behavior, particularly in the presence of open-metal sites, which are a feature of MOFs.[42−44] Indeed, the presence of open-metal sites has been a known modeling complexity in MOFs for over a decade,[45] and various methods have been developed in order to address them.[45−48] Some of these include replacing the Lennard-Jones (LJ) repulsion with a modified Buckingham potential,[45] scaling the typical 12−6 LJ potential with DFT energies,[45,46] as well as modifying the attractive r^{-6} LJ term with an additional r^{-5} to account for higher multipole moments[45] or an additional r^{-4} term to better account for ion-induced dipole interactions.[47,48] Furthermore, dense systems have many-body dispersion effects that require explicit modeling in heterogeneous systems.

Of particular interest in this study is an often used property that has been shown to be problematic in contemporary potential forms: capturing dispersion and its mixing for unlike species, here noble gases.[49] Briefly, the mixing rules of a system dictate how the potential forms of two species will combine to generate the interaction energy between unlikely potential sites. Noble gases conceptually exemplify some of the simplest chemical species, where the ability to capture repulsion and dispersion behavior is isolated from confounding electrostatics and other potential interactions. When mixing rules are applied between unlike noble gases, the resultant dimer potential energies stray dramatically from known values.[1,49] In addition, the highly confined, dispersion-dominated sites in HKUST-1[50] (Figure 1) pose a challenge for the simulation of noble gases.

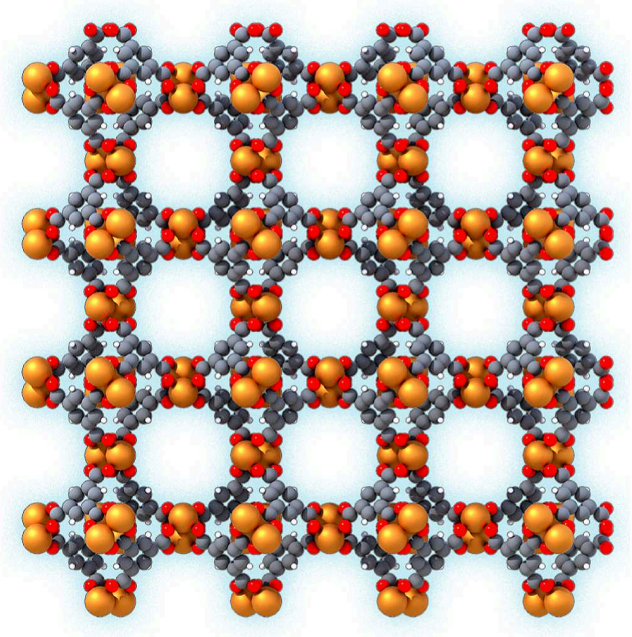

Figure 1. HKUST-1, 2 × 2 × 2 unit cell arrangement. Carbon atoms are represented as gray, hydrogen as white, oxygen as red, and copper as copper/orange.

Thus, with the advent of highly accurate electronic structure calculations, PHAHST (potentials with high accuracy, high speed, and transferability) parameters are fit solely to gas phase electronic structure-derived parameters with a physically motivated form that can subsequently explicitly include many-body interactions as required. It is demonstrated here that the failure of mixing rules appears to be due to the deficiencies in LJ potential forms, and that they work well for PHAHST.[1] That is, if the true homodimer potentials are used, mixing rules are highly effective. On the other hand, if traditional potential functions that are implicitly density-dependent are used, then the mixing rules and transferability are compromised in ways that are neglected in most simulations.

The goal of the PHAHST energy functions is to provide accurate, transferable material modeling through which useful insights into molecular interactions can be gained.[1] Here, PHAHST sorbent−sorbate interactions are explored at a variety of state points chosen to compare with experimental data for krypton and xenon in HKUST-1. PHAHST includes a highly

https://doi.org/10.1021/acs.jctc.4c00226
J. Chem. Theory Comput. 2024, 20, 5570−5582

accurate, theoretically grounded repulsion/dispersion potential energy form coupled with an explicit treatment of polarization and permanent electrostatics. PHAHST is also constructed with the ability to include many-body dispersion.[51] Building upon space group research, the PHAHST force field adds exponential repulsion and improved dispersion terms (relative to prior forms, i.e., PHAST, BSS/BSSP) and stands to offer greatly improved reproduction of short-range structure, yielding enhanced performance in heterogeneous media.[40,51−53] MOFs often present sorbates with a wide variety of interactions and surfaces with distinct spatial environments; therefore, accurately simulating the behavior of sorbates in many diverse environments is a critical test of a model's ability to accurately capture energetics.

HKUST-1 is a microporous and relatively rigid MOF, first synthesized by Chui et al. in 1999.[54] It has been chosen as the material of interest in this work, in part, because it presents a variety of disparate interaction surfaces throughout its interior, which is challenging to accurately model. As seen in Figure 2,

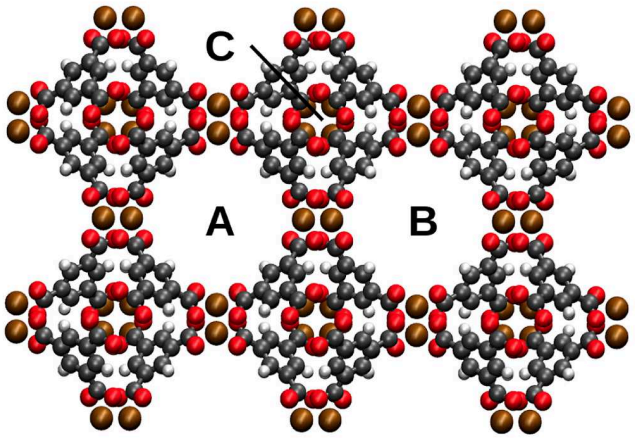

Figure 2. Three distinct pores of HKUST-1.[1] Region (A) is the 13 Å pore with open Cu^{2+} sites, region (B) is the 11 Å pores lined with the organic linker, and region (C) is the 5 Å pore with the octahedral pocket.

HKUST-1 features copper paddlewheel building blocks, composed of copper(II) cations and benzene-1,3,5-tricarboxylate (BTC) linkers. Once assembled, it forms three distinct cages, in which it can sequester guest molecules. The smallest of these is an octahedral pocket with an internal diameter of 5 Å, the walls of which are formed by the flat geometry of four of the BTC linker molecules. These smaller cages connect together to form a three-dimensional rectangular grid, where they act as the vertices. The remaining two cage types appear in an alternating checkerboard fashion throughout the spaces formed by the rest of the grid. The larger cage has a diameter of approximately 13 Å, whereas the smaller cage has a diameter of roughly 11 Å. All of the material's open-metal sites appear lining the interiors of the 13 Å cage. Thus, the cages include equal numbers of similar size and readily accessible cavities with interactions that are distinctly repulsion/dispersion dominated or include available open-metal sites.

HKUST-1 has previously been considered for use as a final step for krypton/xenon separation following a procedure that results in an 80:20 molar ratio of krypton to xenon separated at 273 and 298 K.[25,55] The heterogeneous pore environment in HKUST-1, presumably responsible for this critical separation, presents a challenge to typical LJ force fields. This is due to the poor representation of the repulsion as a power law,[56−58] missing important contributions from higher-order dispersion interactions,[59,60] and neglecting explicit many-body polarization.[2,61−64] Additionally, commonly used LJ mixing rules produce inaccurate well depths between distinct species.[49] As a result, an improved potential that handles these contributions fundamentally better, i.e., the PHAHST force field,[1] is rigorously tested in a highly diverse environment at state points that have been explored experimentally due to their technological relevance.

METHODS

Krypton and xenon simulations in HKUST-1 used the PHAHST parameters previously developed by Hogan and Space.[1] Simulations were performed using GCMC in MPMC[65] to model gas behavior at a variety of thermodynamic conditions to match experimental data. Additionally, pair potentials were calculated using CCSD(T) at the aug-cc-pVQ/5Z-PP level of theory and compared to PHAHST and LJ potentials testing different mixing rules as well as two modifications to the LJ potential (section). The three pair potentials were Kr−Kr, Kr−Xe, and Xe−Xe.

PHAHST Force Field. The most recent iteration of force fields used by the Space research group was developed by Hogan and Space.[1] Building on the previous generation of force fields by our group, improvements provided by the PHAHST model include exponential repulsion and three leading, asymptotically correct dispersion coefficients. The potential forms are developed by fitting these parameters directly via accurate electronic structure calculations in order to capture relevant intermolecular interactions with chemical accuracy.[1] This procedure creates an accurate and transferable framework with which to build reliable potentials amenable to further elaboration.

Specifically, considering the contributions to the potential energy at typical equilibrium intermolecular interaction distances, PHAHST exponential forms capture the repulsive energy contribution better than the r^{-12} term used in LJ potential forms,[66] while the LJ r^{-6} dispersion term typically accounts only for approximately 60% of the total dispersion energy at distances comparable to van der Waals contact, and PHAHST includes higher-order terms.[67] Additionally, in many extant LJ applications, the mixing rules used are geometric on the well-depth parameter, ϵ, and not on the dispersion coefficient itself, which has a more physical foundation for mixing. As a result, the LJ mixing rules used are known to be highly inaccurate, especially between species with a disparate number of electrons.[49] While the common choice offers no practical or theoretical advantage, it has been propagated as a legacy choice for decades. However, the simple physical mixing rules are highly effective for the physically motivated PHAHST potential form.

The complete PHAHST force field, here omitting many-body dispersion, calculation takes the form

$$U_{\mathrm{PHAHST}} = U_{\mathrm{rd}} + U_{\mathrm{el}} + U_{\mathrm{pol}} \quad (1)$$

which sums contributions from repulsion/dispersion, permanent electrostatics, and many-body polarization, respectively. The repulsion/dispersion form, U_{rd}, is quantified as[67]

https://doi.org/10.1021/acs.jctc.4c00226
J. Chem. Theory Comput. 2024, 20, 5570−5582

$$U_{rd} = \sum_{i \neq j} \frac{F_0}{\beta_{ij}} e^{\beta_{ij}(r_{ij} - \rho_{ij})} + \sum_{n=3}^{5} f_{2n}(\beta r_{ij}) \frac{C_{2n}}{r_{ij}^{2n}} \quad (2)$$

where β_{ij} is the exponential range parameter, ρ_{ij} is the distance at which the repulsive force is equal to F_0 (chosen to be 10^{-3} au), C_{2n} is the $2n$th asymptotically correct dispersion coefficient, and $f_{2n}(\beta r_{ij})$ is a damping function of the form

$$f_{2n}(\beta r_{ij}) = 1 - e^{-\beta r_{ij}} \sum_{k=0}^{2n} \frac{(\beta r_{ij})^k}{k!} \quad (3)$$

which is that of an incomplete gamma function derived from the semiclassical Drude model first proposed by Tang and Tonnies.[59] Here, β_{ij} is the same parameter that appears in eq 2, as both quantify the extent of wave function overlap.

A geometric average is used for the dispersion coefficient mixing rules[59,67,68]

$$C_{2n,ij} = \sqrt{C_{2n,ii} C_{2n,jj}} \quad (4)$$

while the repulsion mixing rules arise from a distortion model of electronic densities, constrained so that the intermediate surface terminates to be approximately planar.[69] Minimizing the distortion energy results in equal and opposite restoring forces in each atom. The repulsion form simplifies the chosen mixing rules to the arithmetic average of the distance parameter

$$\rho_{ij} = \frac{1}{2}(\rho_{ii} + \rho_{jj}) \quad (5)$$

and the harmonic average of the range parameter

$$\beta_{ij} = 2\frac{\beta_{ii}\beta_{jj}}{\beta_{ii} + \beta_{jj}} \quad (6)$$

The permanent electrostatic energy, U_{es}, is calculated between pairs of partial point charges using Coulomb's law with Ewald summation where appropriate[70]

$$U_{el} = \sum_{i \neq j} k_e \frac{q_i q_j}{r_{ij}} \quad (7)$$

PHAHST treats many-body polarization energy explicitly, using a Thole–Applequist-type model.[71,72] In the present work, polarization energy was determined to play a small role in the energetics of this system, so the discussion herein will be limited; however, readers wishing for more detail are encouraged to acquaint themselves with previous studies.[70−72] Briefly, the model assigns each chosen site a scalar point polarizability whose behavior is then determined by many-body polarization equations. A dipole field tensor is constructed, which characterizes each dipole's response to the static electric field, such that each site in this tensor is itself a 3 × 3 tensor. The product of this dipole field tensor with the system dipoles produces their contribution to the electric field, a contribution that in turn induces slightly different dipoles. This calculation is then repeated and typically iterated until convergence to a self-consistent electric field and dipole set is realized, although direct solution via matrix inversion is also possible. Potentials that lack the ability to explicitly and reliably model many-body polarization cannot assess the relative importance of the open-metal sites. For example, hydrogen sorption in HKUST-1 is first sorbed onto the open-metal sites, guided by the electrostatic interactions aided by hydrogen's quadrupole. Here, the rare gases interact strongly with the open-metal sites via polarization, but they are not the most favorable sorption interactions compared to the dispersion-dominant sites. Thus, it is necessary to include polarization to rule it out as the most favorable sorption location given the highly polarizable sorbates and to capture the relative populations.

Potential Parameterization. Potential parameters for krypton, xenon, and HKUST-1 were taken from Hogan and Space,[1] where the procedure for establishing each is discussed in detail—sorbate and sorbent potential parametrization require different methods given the disparate system sizes and the use of electronic structure methods that scale unfavorably with the number of electrons considered. The PHAHST model requires determination of two repulsion parameters, three dispersion coefficients, static dipole polarizability, and partial atomic charges. For the noble gases, the C_6 and C_8 dispersion coefficients as well as the static polarizability were calculated using the Williams–Stone–Misquitta technique via the CamCASP software suite, while the C_{10} dispersion coefficient can be computed directly from the C_6 and C_8 coefficients. Atomic partial charges were computed using the electronic structure code ORCA, using the orbital-optimized coupled cluster singles' and doubles' density via the standard CHELPG method.[73−76] The exponential repulsion parameters were fit to high-quality dimer surfaces taken from the literature using the surface fitting routines in the MPMC simulation software.[51,52,77,78] The procedure for parametrization of HKUST-1 is complicated by the number of atoms in its unit cell. It involves division of the MOF into arbitrary, though carefully chosen, fragments which are small enough to be computationally tractable—although these fragments are still too large to be treated to the same level of theory to which the sorbates were subject.

Grand Canonical Monte Carlo. Single isotherm simulations of krypton and xenon were modeled from 0.1 to 1.0 atm at 292 K. These simulations parameters were chosen to verify our model against previously published research by Perry et al.[79] Additionally, a series of simulations were performed at 273 and 298 K under pressures ranging from 0.001 to 10 atm in an environment of krypton and xenon in an 80:20 molar ratio, respectively. This ratio and temperature range were selected in order to simulate industrial conditions as described in previous work by Ryan et al.[25] and Bae et al.[80] Each simulation was run for 6 million equilibration steps, followed by 6 million production steps, where samples were taken once each sorbate molecule had been successfully perturbed, on average, at least twice as determined by uptake and acceptance rate. Averages were observationally converged as well. Monte Carlo moves consisted of insertion, deletion, and translations. Preliminary tests in the form of single component uptake simulations indicated that the polarization energy played a negligible role in the behavior of these systems. Since explicit many-body polarization is a computationally expensive calculation, it is best avoided when possible. To test the importance of polarization, three state points were selected—the lowest, intermediate, and highest pressures for each temperature—where polarization was enabled. When it was determined that the energy from polarization was less than 1% of the total energy, no further polarized simulations were conducted. Note that despite the apparent lack of energy contribution from polarization, the many-body nature of the polarization does play a role here. The slightly large open-metal site cavity indeed has significant metal-induced dipoles based on the charges and polarizabilities involved; however, the symmetry of the metals, see, e.g., Figure

https://doi.org/10.1021/acs.jctc.4c00226
J. Chem. Theory Comput. 2024, 20, 5570−5582

1, in the cavity leads to cancellation of the total dipole with polarization, contributing less than one percent of the total energy.[1]

In addition to isotherm simulations, the selectivity of xenon over krypton was examined and compared to experimental data.[79−82] Selectivity was calculated in two ways: statically and dynamically.

Static calculations used Henry's law

$$n = k_H P \tag{8}$$

where n is the amount of gas adsorbed, k_H is Henry's constant, and P is the pressure of the system. Henry's constant is obtained by fitting a linear regression using eq 8, where k_H is the slope of the line. Because Henry's law only applies to sufficiently dilute systems, extremely low pressure points must be simulated. Pressure points ranged from 0.3 to 2.0 mbar at 280 and 310 K, which matched experiment by Soleimani Dorcheh et al.[82] The ratio of Henry's constant for each gas is then compared

$$S_{static} = \frac{k_{H,Xe}}{k_{H,Kr}} \tag{9}$$

which gives the ideal selectivity of xenon over krypton. While other methods of obtaining k_H directly from simulation exist,[83,84] calculations were done in this manner in order to match experiment.[82]

Dynamic calculations were done with a standard definition[80]

$$S_{dynamic} = \frac{x_{Xe}}{x_{Kr}} \cdot \frac{y_{Kr}}{y_{Xe}} \tag{10}$$

where x and y are gas phase mole fractions of the absorbed and bulk phase, respectively. These calculations were matched with experimental data that integrated an 80:20 ratio of krypton to xenon from breakthrough curves.[80,81]

The isosteric heat of adsorption (Q_{st}) is defined as the heat released when an adsorptive bond binds to a surface. The larger the magnitude, the more favorable the interaction, which helps intuit the selectivity of the gas. For a single component, Q_{st} is calculated directly from the statistical mechanical fluctuations of the average number of particles, $\langle N\rangle$, and average energy, $\langle U\rangle$[85]

$$Q_{st} = -\frac{\langle NU\rangle - \langle N\rangle\langle U\rangle}{\langle N^2\rangle - \langle N\rangle^2} + k_B T \tag{11}$$

where $\langle\cdots\rangle$ represents the ensemble average, k_B is Boltzmann's constant, and T is temperature in Kelvin. Q_{st}^0 was also examined by Canonical (NVT) ensemble simulations. In this case, the guest particle in the simulation box was constrained to 1 and calculated via the formula[86]

$$\Delta H = Q_{st}^{\ 0} = \langle U\rangle + k_B T \tag{12}$$

For a binary mixture, the Q_{st} for component i can be obtained from simulations via the following equations[87,88]

$$Q_{st,i} = RT - \left(\frac{\partial U^{a,c}}{\partial N_i^a}\right)_{T,V^a,N_{j\neq i}^a} \tag{13}$$

which is the ideal behavior of bulk fluid. The superscripts a and c represent the adsorbed and ideal phases, respectively. The partial derivative can be expanded by

$$\left(\frac{\partial U^{a,c}}{\partial N_i^a}\right)_{T,V^a,N_{j\neq i}^a} = \sum_k \left(\frac{\partial U^{a,c}}{\partial \beta\mu_k}\right)_{T,V^a,N_{j\neq i}^a} \left(\frac{\partial \beta\mu_k}{\partial N_i^a}\right)_{T,V^a,N_{j\neq i}^a} \tag{14}$$

where the first term can be described by direct numerical integration of the configurational internal energy or by using fluctuation theory

$$\left(\frac{\partial U^{a,c}}{\partial \beta\mu_k}\right)_{T,V^a,N_{j\neq i}^a} = f(U, N_k^a) \tag{15}$$

Here, the notation $f(X, Y) = \langle XY\rangle - \langle X\rangle\langle Y\rangle$ stands for the fluctuations of any X−Y pair. The $\partial\beta_{\mu k}/\partial N_i^a$ partial derivative takes the form of the linear algebraic equation

$$\mathrm{FX} = \mathbf{I} \tag{16}$$

where $\mathbf{F} = f(N_i^a, N_j^a)$, $\mathbf{X} = (\partial\beta\mu_i/\partial N_j^a)$, and $\mathbf{I}$ is the identity matrix. Following a matrix inversion, the binary mixture is obtained

$$\begin{pmatrix} \frac{\partial\beta\mu_1}{\partial N_1^a} & \frac{\partial\beta\mu_1}{\partial N_2^a} \\ \frac{\partial\beta\mu_2}{\partial N_1^a} & \frac{\partial\beta\mu_1}{\partial N_2^a} \end{pmatrix} = \begin{pmatrix} f(N_1^a, N_1^a) & f(N_1^a, N_2^a) \\ f(N_2^a, N_1^a) & f(N_2^a, N_2^a) \end{pmatrix}^{-1} \tag{17}$$

Finally, pair potentials for three combinations of krypton/xenon were examined in order to ascertain any discrepancies observed between the models using CCSD(T) at the aug-cc-pVQ/5Z-PP level of theory and compare it to both PHAHST and LJ. The combinations are Kr−Kr, Kr−Xe, and Xe−Xe.

Lennard-Jones Mixing Rules. As discussed previously, mixing rules for the LJ potential between disparate noble gases produce inaccurate well depths. Here, we examine two: Lorentz−Berthelot (LB), by far the most common mixing rule[89]

$$\sigma_{ij} = \frac{\sigma_{ii} + \sigma_{jj}}{2};\ \epsilon_{ij} = \sqrt{\epsilon_{ii}\epsilon_{jj}} \tag{18}$$

and C_6 mixing, proposed by Hudson and McCoubrey[90]

$$\sigma_{ij} = \frac{\sigma_{ii} + \sigma_{jj}}{2};\ \epsilon_{ij} = 2^6 \frac{\sigma_{ii}^3 \sigma_{jj}^3}{(\sigma_{ii} + \sigma_{jj})^6} \sqrt{\epsilon_{ii}\epsilon_{jj}} \tag{19}$$

The difference in these mixing rules lies in ϵ_{ij}. Despite the ubiquity of LB mixing rules among molecular simulations, the use of the LB ϵ_{ij} term is not sound for simulations with distinct species. The only circumstance in which the LB ϵ_{ij} term is true is when $\sigma_{ii} = \sigma_{jj}$, and the first factor in eq 19 becomes unity.[90] C_6 geometric mixing is a more sound choice that mixes the r^{-6} coefficient in the LJ potential, where $C_6 = 4\epsilon\sigma^6$. Equation 19 examines this choice where the equation is obtained by direct substitution, e.g., using $\sigma_{ij} = (\sigma_{ii} + \sigma_{jj})/2$, without further approximation. The choice of LB and C_6 mixing rules offers a comparison between a mixing rule that is primarily driven by legacy and one that is more theoretically grounded. Nonetheless, it will be demonstrated that the true pair potentials can be mixed simply and accurately, and the effective nature of LJ potentials is not easily mixed reliably.

Lennard-Jones Modifications. In addition to examining different mixing rules, both the C_6 dispersion term, as described by the second term in eq 2, and the repulsive C_{12} term, as described by the first term in (2), were fit to the LJ potential to

https://doi.org/10.1021/acs.jctc.4c00226
J. Chem. Theory Comput. 2024, 20, 5570−5582

see that the LJ potential is piecewise improvable. The modified potentials take the following forms

$$U_{LJ}^{C_6} = 4\epsilon\left(\frac{\sigma}{r}\right)^{12} - f_6(\beta r_{ij})\frac{C_6}{r_{ij}^6} \tag{20}$$

where the damping function, $f_6(\beta r_{ij})$, is described by eq 3, and

$$U_{LJ}^{C_{12}} = \sum_{i\neq j}\frac{E_0}{\beta_{ij}}e^{\beta_{ij}(r_{ij}-\rho_{ij})} - 4\epsilon\left(\frac{\sigma}{r}\right)^6 \tag{21}$$

where the terms in the first portion of (21) are the same as in (2).

It is well-known that the attractive term in the LJ potential (r^{-6}) is physically grounded (i.e., London dispersion forces), and the repulsive term (r^{-12}) is simply the square of the attractive term, a method done for computational efficiency when computing resources were scarce. The modifications presented above test both portions of the LJ potential. The justification is that altering the standard LJ C_6 with the ab initio C_6 in eq 20 should produce asymptotic dispersion. Conversely, altering the LJ C_{12} with the exponential term in eq 21 should produce more accurate repulsions than the standard 12−6 LJ potential. In short, the exchange of the LJ terms with the previously described terms from eq 2 will elucidate the importance of exponential repulsion and/or higher-ordered dispersion terms when modeling noble gases.

RESULTS AND DISCUSSION

Single Isotherms. The PHAHST simulations at 292 K were performed with a gas reservoir entirely of krypton or xenon. The

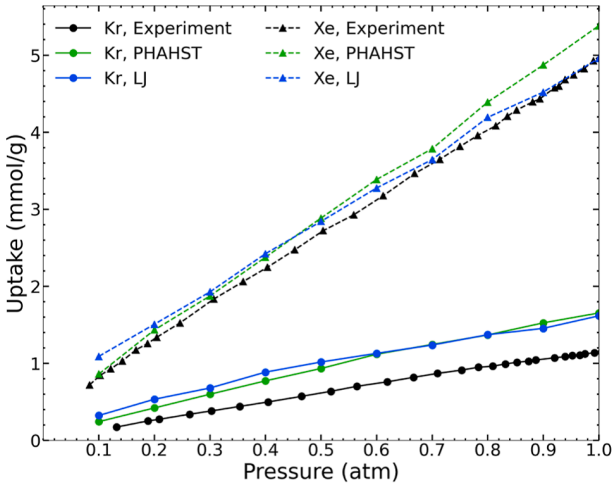

Figure 3. Simulated Kr and Xe isotherms for HKUST-1 at 292 K in a pure gas environment. Kr is represented by solid lines with circle markers and Xe by dashed lines with triangle markers. PHAHST (green) is compared to LJ (blue) and experimental (black) results from the literature.[79]

Table 1. Henry's Constants for Krypton and Xenon

	Henry's constants ($cm^3\ g^{-1}\ kPa^{-1}$)					
	krypton			xenon		
temp. (K)	exp[82]	PHAHST	LJ	exp[82]	PHAHST	LJ
280	0.39	0.44	0.17	4.59	4.76	2.32
310	0.18	0.16	0.06	1.50	1.28	0.64

Table 2. Static Selectivity for Xe/Kr Ratios Calculated via Equation 9

	Xe/Kr static selectivity		
temp. (K)	exp[82]	PHAHST	LJ
280	11.8	10.8	14.0
310	8.7	7.8	11.2

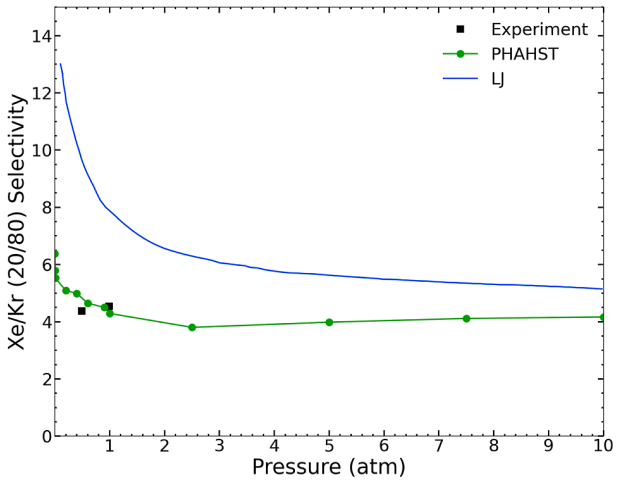

Figure 4. Xe/Kr selectivity (20:80 mixture) in HKUST-1 at 298 K by PHAHST model (green) and LJ (blue) reported by Bae et al.[80] Experimental data points (black squares) reported in the same work.[80]

Table 3. Xe/Kr (20:80) Selectivity in HKUST-1 at Experimentally Relevant State Points[a]

	Xe/Kr selectivity		
pres./temp[b]	exp	PHAHST	LJ
1 mbar/280 K	11.8[82]	10.8	14.0
1 mbar/310 K	8.7[82]	7.8	11.2
0.01 atm/292 K	6.9[79]	6.8	9.0[79]
0.5 bar/298 K	4.4[80]	4.5	9.7[80]
1 bar/273 K	2.6[81]	4.7	8.1[25]
1 bar/298 K	4.5[80]	4.3	7.9[80]

[a]Data points at 1 mbar are calculated via Henry's constant (eq 8). Remaining data points are calculated dynamically (eq 10). LJ results without citations had no known literature values and were obtained by our simulations. [b]Pressure and temperature points are reported as stated by experiment.

simulations show comparable agreement with both experimental and LJ results from a previous study.[79] Results are plotted in Figure 3. Due to its simplicity, the LJ model is well-known for its accuracy of modeling simple fluids and gases, e.g., dispersively interacting spherical particles. The results here indicate that the PHAHST force field performs comparably with the LJ model in this environment. Such comparisons are useful to validate any newly created force field and demonstrate the efficacy. In addition, the speed of the calculations performed was nearly identical, with the LJ calculations taking an average of 0.018 s/step and the PHAHST calculations taking an average of 0.019 s/step. Without many-body polarization, the choice of the LJ potential is not a significant computational advantage.

Despite matching experimental data, however, the results from the LJ potential are less physically grounded. The LJ potential is density-dependent with implicit many-body effects fit to reproduce bulk data and performs unpredictably in an

https://doi.org/10.1021/acs.jctc.4c00226
J. Chem. Theory Comput. 2024, 20, 5570−5582

Table 4. Contribution of Energetics for the PHAHST and LJ Force Fields[a]

	Kr/Xe energy contributions (K)						
method	U_{rd}	%	U_{el}	%	U_{pol}	%	U_{total}
PHAHST	−45318.06	99.4	0.0	0.0	−258.82	0.6	−45576.88
LJ	−52255.79	99.7	0.0	0.0	−153.43	0.3	−52409.22

[a]Energy is taken from the state point at 1.0 atm and 298 K.

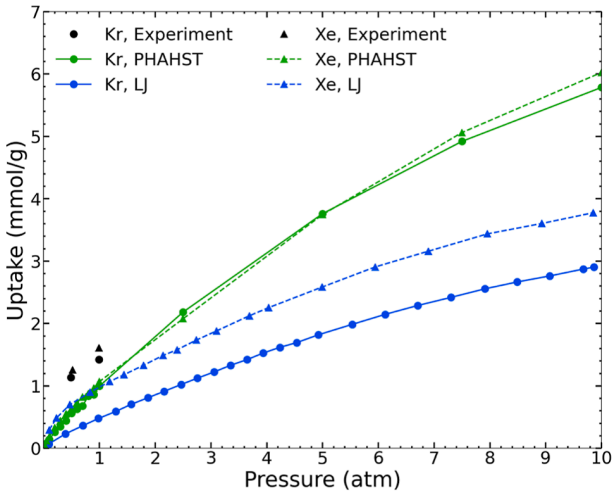

Figure 5. Simulated and experimental krypton and xenon adsorption isotherms at 298 K in an 80:20 molar gas reservoir. PHAHST (green) compared to LJ (blue) and experiment (black) from Bae et al.,[80] with krypton and xenon represented by circles and triangles, respectively. Experimental adsorption values were obtained by integrating the values from breakthrough experiments.

Table 5. Molar Ratios of the Uptake of Xe/Kr (20:80) at 298 K[a]

	Xe/Kr	
	~0.5 atm	~1 atm
exp	1.11	1.13
PHAHST	1.07	1.17
LJ	2.60	2.17

[a]Experimental data and values for the LJ model were both in the published results of Bae et al.[80]

interfacial environment. Furthermore, the r^{-6} accounts for only 60% of the true potential energy of a system, so it needs to be overrepresented via LJ potentials.[67] To compensate for this deficiency, the r^{-6} term is then fit to the bulk experimental data. As a result, the results presented above do not represent the microscopic energetic behavior of krypton nor xenon in HKUST-1. Because the PHAHST parameters are obtained from ab initio data,[1] the results it obtains are physical and represent an improvement in simulation quality for single component isotherms and can, for example, be used to calculate energy decompositions in a meaningful fashion.

Henry's law coefficients were calculated and found to match the experiment by Soleimani Dorcheh et al.[82] at the low pressure region of 0.3 to 2.0 mbar.[82] Derived Henry's constants are in Table 1, and calculated static selectivity is presented in Table 2.

Mixed Isotherms. Mixed isotherm simulations were performed at 273 and 298 K in a molar environment of 80% krypton and 20% xenon. An additional dynamic selectivity calculation was performed at 292 K. Molar ratios were chosen to be compared to experimental values, which themselves derive

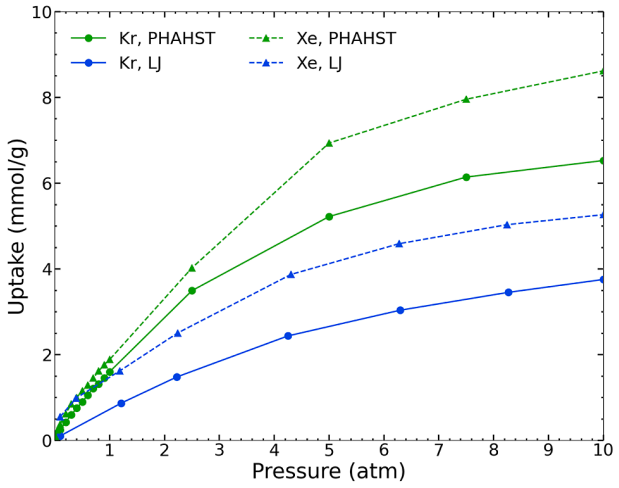

Figure 6. Simulated Kr/Xe (80:20) adsorption isotherms in HKUST-1 at 273 K. Krypton uptake is represented by solid lines and xenon by dotted lines. Simulations were performed with the PHAHST model (green) and the LJ model (blue) as reported by Ryan et al.[25]

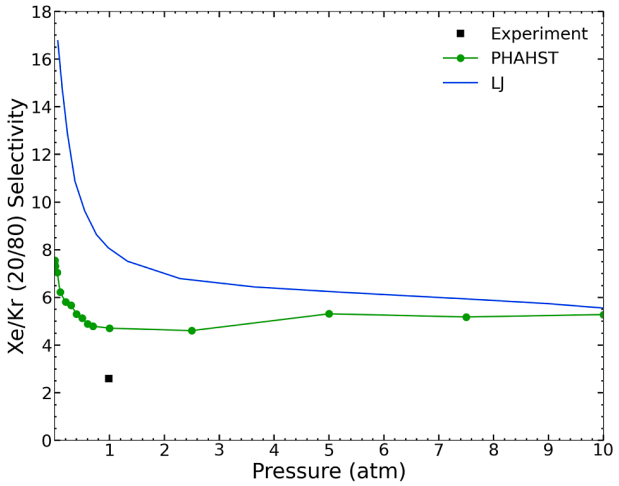

Figure 7. Simulated and experimental Xe/Kr (20:80) selectivity in HKUST-1 at 273 K using the PHAST model (green) and the LJ model (blue) as reported by Bae et al.[80] Experimental result (black square) from like conditions as reported by Liu et al.[81]

Table 6. Isosteric Heats of Adsorption at Zero Loading[a]

	Q_{st}^0 (kJ/mol)	
method	Kr	Xe
exp	18.7	26.9
DFT	19.7	27.1
PHAHST	19.6	26.4
LJ	23.1	32.6

[a]Simulated results are compared to experimental results from Soleimani Dorcheh et al.[82]

https://doi.org/10.1021/acs.jctc.4c00226
J. Chem. Theory Comput. 2024, 20, 5570−5582

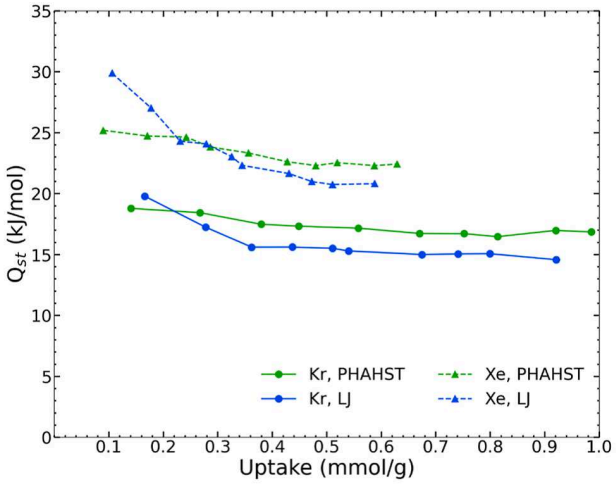

Figure 8. Simulated Q_{st} for Kr/Xe (80:20) with the PHAHST model (green) and the LJ model (blue); Kr represented by circles, xenon represented by triangles.

their respective ratios from cryogenic distillation of the atmosphere. Results can be seen in Figure 4 of the state points at 0.5 and 1.0 bar at 298 K from Bae et al.,[80] and a comparison of all experimental and simulated selectivity data can be seen in Table 3.

As demonstrated, PHAHST shows remarkable agreement with the known experimental selectivity, outperforming the LJ potential in all cases. Of note, the LJ potential shows a dramatic oversorption of krypton and xenon, a trend that is consistent with all simulations performed. This is due to the overfitting of the dispersion term and the reliance on electrostatics that is typical with the LJ potential. Seen below, in Table 4, the repulsion/dispersion energy contributions for over 99% of the total potential energy in the simulation, indicating that any improvement seen compared to PHAHST and LJ is strictly due to the newly implemented repulsion/dispersion form (eq 2).

In the mixed-sorbate uptake simulations (Figure 5), PHAHST predicted that both gases would be readily adsorbed with roughly even uptake of each gas. This is an observation of note considering the substantial excess of krypton over xenon in

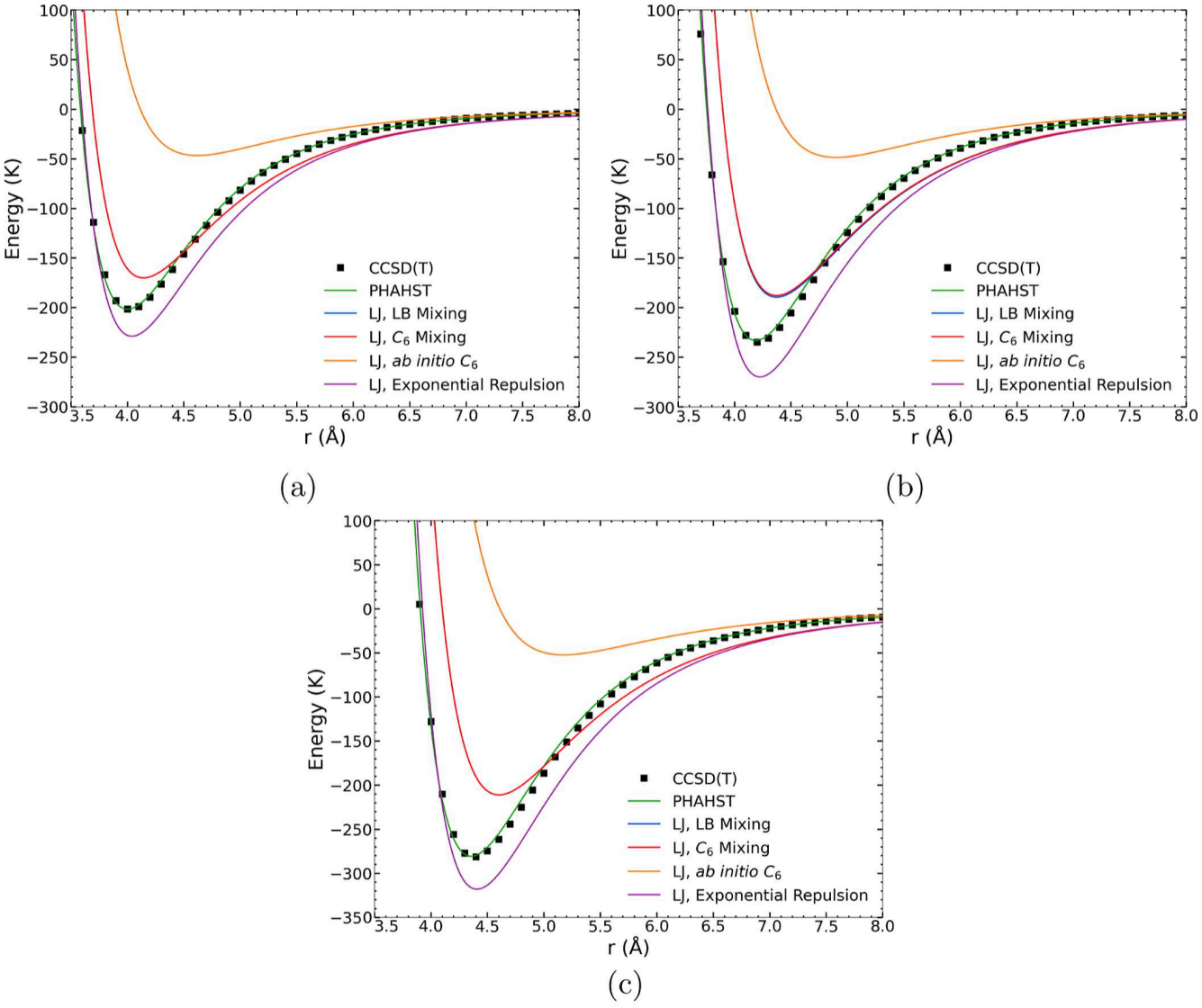

Figure 9. Pair potentials for Kr−Kr (a), Kr−Xe (b), and Xe−Xe (c). Calculations used CCSD(T) at the aug-cc-pVQ/5Z-PP level of theory (black squares), the PHAHST model (green), and the LJ model (blue, red, and orange for respective mixing rules).

https://doi.org/10.1021/acs.jctc.4c00226
J. Chem. Theory Comput. 2024, 20, 5570−5582

Table 7. Well-Depth Energy for Krypton and Xenon Pair Potentials from Figure 9[a]

	pair potential well-depth energy (K)					
method	Kr−Kr	% Dev	Kr−Xe	% Dev	Xe−Xe	% Dev
CCSD(T)	−201.69		−234.84		−281.43	
PHAHST	−201.56	0.067	−233.12	0.73	−280.58	0.30
LJ (LB mixing)	−170.00	15.72	−189.39	19.35	−211.00	25.03
LJ (C_6 mixing)	−170.00	15.72	−187.82	20.02	−211.00	25.03
LJ (ab initio C_6)	−46.64	123.12	−48.56	79.32	−52.25	118.57
LJ (exp rep.)	−222.92	10.53	−269.43	14.73	−317.90	12.96

[a]Energy is in Kelvin. Percent deviations are compared to CCSD(T).

the simulated surroundings, a trend that is noticeably absent in the LJ model. The uptake predicted for each gas was a close match with the experiment, compared to the values reported by Bae et al.[80] on the order of 0.5 mmol/g at both state points for which data was available.

Both PHAHST and LJ simulations at 298 K predicted less krypton/xenon uptake than was reported experimentally, although both were within 1 mmol/g of the measured values in absolute terms. Of greater interest is the relative uptake of each gas. In this context, PHAHST was a remarkably tight fit, with krypton/xenon ratios deviating from experiment by ∼3.6% at both state points for which data was reported (Table 5). The standard LJ model predicted a significant excess of xenon over krypton in the adsorbed phase, resulting in selectivity that was dramatically higher than that in experiment; by contrast, the PHAHST model predicts selectivity directly in line with the experimental measurements (Figure 4). At 0.5 atm, for example, the empirical result was 4.4, while PHAHST gives a value of 4.8. The standard LJ models predict a much higher level of Xe/Kr selectivity, with Bae et al. reporting a value of 12.[80]

The PHAHST simulations at 273 K were performed with the same 80:20 krypton/xenon molar ratio. The simulations predicted that both gases would be readily adsorbed across the entirety of the simulated pressure range; however, the amount of xenon observed in the interior of the crystal exceeded that of krypton at all pressures examined. The krypton/xenon ratio peaked at initial loading, where its molar uptake was almost twice that of krypton, despite xenon being outnumbered 4 to 1 in the simulated environment (Figure 6). From there, the ratio of xenon to krypton rapidly decreased with rising pressure, dropping to 1.2 by the time the system reached 0.5 atm. With further increases in pressure, the uptake of both gases rose in proportion, allowing the system to roughly maintain this relative composition throughout the remainder of the simulated state points.

In a 2008 paper, Ryan et al.[25] modeled this system using the standard LJ potential form (Figure 6).[25] Compared to this model, the PHAHST predicts a slightly greater level of adsorption for both gases in absolute terms. In relative terms, at the high end of the pressure range, both models agree that the molar uptake of xenon should exceed that of krypton by about 25%. However, at lower pressure and under conditions where dispersion effects are more significant, PHAHST exhibits a much more even uptake of both gases, whereas the LJ modeling suggests xenon uptake will exceed krypton adsorption substantially, such that the observed krypton/xenon uptake ratio is ∼1.7 times higher in the LJ model as compared to PHAHST. Consequently, the low-pressure selectivity predicted by PHAHST is reduced by an equivalent factor (Figure 7).

In a later work, Liu et al. would perform breakthrough experiments running an 80:20 krypton/xenon mixture through HKUST-1 at 273 K and 1 bar.[81] By integrating the area above their breakthrough curves, they calculated a selectivity of 2.6 for xenon over krypton. This value is somewhat lower than the PHAHST prediction of 4.7, but it is much lower than the selectivity of 8.1 in the LJ model (Figure 7).[25] Liu et al. theorized that the difference between LJ and experiment could be largely attributed to kinetic effects on selectivity; however, Bae et al. speculated that the smaller octahedral pores were blocked due to a lower Brunauer−Emmett−Teller (BET) surface area than expected.[80] PHAHST affirms that this is the likely scenario, given the previous agreement with all other selectivity reference points (Table 3).

Isosteric Heats of Adsorption. The low loading (Q_{st}^0) isosteric heat of adsorption for single component simulations and multisorbate isosteric heats of adsorption (Q_{st}) for krypton and xenon were examined. Q_{st}^0 results can be seen in Table 6.

DFT simulations were performed with CP2K[91] utilizing the MOLOPT basis set[92,93] at the TZVP level for all atoms. GTH pseudopotentials[93] were used to describe core electrons with the PBE functional used for the exchange−correlation energy.[94] The geometry of the gas was first optimized, and then the binding energy was calculated with corrections applied for basis set superposition error using the counterpoise method.[95]

The canonical (*NVT*) ensemble was used for both PHAHST and LJ simulations, which constrains the number of particles in the simulation to a single gas atom in the MOF. Classical simulations were performed at temperatures to match the experimental range of Q_{st}^0 values[82] (T = 280 and 310 K for krypton and xenon, respectively) and calculated via eq 12.

From the values in Table 6, PHAHST outperforms the LJ potential for both krypton and xenon at zero loading, agreeing well with both experimental and DFT results. It is expected that minimized DFT will demonstrate a more favorable binding site than experiment as the temperature of the system approaches absolute zero. Regardless, the agreement between the DFT and PHAHST is notable. The sorbate positions in the pore in all cases were similar; however, the LJ model energy is off by nearly 20% for both krypton and xenon.

The LJ krypton and xenon pair potentials are not as attractive as the true potential (section), which leads to unpredictable fidelity with respect to krypton/xenon sorption as the energy values are lower. Because noble gas sorption is a balance between repulsion and dispersion forces, using an inadequate functional form fails in an unpredictable manner. This incorrect functional form is an unforced error in simulation models.[70]

To investigate mixed gas sorption, multisorbate Q_{st} was calculated via 13 to compare performance at 298 K. Note that while it is challenging to extract partial molar enthalpy experimentally, they are given directly in GCMC via the fluctuations of $\langle N \rangle$ and $\langle U \rangle$, although this formalism has rarely been used in the literature. Figure 8 demonstrates that the

https://doi.org/10.1021/acs.jctc.4c00226
J. Chem. Theory Comput. 2024, 20, 5570−5582

PHAHST multisorbate model shows a slight decrease in Q_{st} with loading. As the gas loads into the MOF, somewhat less favorable sites are available, and Q_{st} decreases slowly and nearly constantly by ∼2 kJ/mol over the range considered. The LJ model shows a more dramatic decrease in Q_{st}, with krypton decreasing by ∼5 kJ/mol and xenon decreasing by ∼7 kJ/mol. This change in Q_{st} is supported by the selectivity in Figure 4, where the PHAHST model shows a slight initial decrease before leveling off, whereas the LJ model shows an initial dramatic decrease before continuing a slow decent.

Pair Potentials. Another implication here is that while the LJ model appears to calculate the correct answer when performing a pure gas simulation (Figure 3), the pair potentials demonstrate that the LJ model is off significantly and in an unpredictable manner with like atom effective potentials and the inability to accurately mix. The "correct" answer calculated by the LJ model is more likely due to cancellation of error, something that is not new to results produced by the LJ potential.[96] This is seen when selectivity calculations are performed (Figure 4) and when the errors produced by the LJ model become pronounced, demonstrating that the previously described repulsion/dispersion parameters (eq 2) are required to accurately calculate the total energy in these molecular systems.

As seen in Figure 9a,c, the LJ lines for LB and C_6 mixing are exact. This behavior is expected, as the mixing rule terms in eqs 18 and 19 for *ii* and *jj* are the same. For Figure 9b, a slight distinction can be seen for Kr−Xe mixing for both types of mixing rules. However, it is demonstrated that the LJ pair potential is unable to reproduce the pair potential from CCSD(T). This is because the LJ parameters are largely trained on bulk experimental data for specific state points,[34−39] and as a result are unable to reproduce the correct pair potential when removed from their training environment.

Because PHAHST is explicitly parametrized solely to ab initio data, it is not only able to accurately reproduce the result from CCSD(T) (Table 7) but it is capable of matching experimental data in a completely different environment. This is due to its explicit calculation of the exponential repulsion, as well as the C_6, C_8, and C_{10} terms.

To test whether or not the LJ potential can accurately capture CCSD(T) data, the PHAHST ab initio C_6 and exponential repulsion were tested in conjunction with the LJ potential, as described previously by eqs 20 and 21. Here, ab initio C_6 is represented by the orange lines, and exponential repulsion is represented by the purple lines. From Figure 9 and Table 7, the ab initio C_6 in the LJ potential severely underestimates the dispersion energy. This is because, when parametrizing the LJ to bulk experimental data, the higher-ordered dispersion coefficients (C_8 and C_{10}) are implicitly included with the LJ C_6 term. As a result, the dispersion terms become overly represented in the standard 12−6 LJ potential, which can be seen with the purple lines in eq 21. In the purple line, correcting for exponential repulsion reveals an overly favorable pair potential. Therefore, it is not enough to simply "fix" each portion of the LJ equation, but it is necessary to rebuild the potential from the ground up. An upcoming publication will explore these pair potentials further for all noble gases.

CONCLUSIONS

In this study, we performed grand canonical Monte Carlo simulations on the noble gases krypton and xenon. Gas uptake was modeled in the MOF, HKUST-1, which presents a highly heterogeneous surface for interaction with its guest molecules and atoms. In addition to having pores and cages in a variety of sizes, HKUST-1 also has open-metal sites in the interior of one of its chamber types. Not only is this MOF challenging to model but also the sorbates themselves have proven to be problematic in the past. Traditional force fields have relied on the electrostatic energy to obtain correct modeling, while dispersion-dominated interactions have been known to fail acutely. Furthermore, the mixing rules, when applied to noble gases, often prove to be equally inaccurate. All of these factors, taken together, indicate that modeling this combination of MOF and mixed sorbates should be a daunting task. However, the new models have demonstrated a remarkable level of success.

The adsorption isotherms at 298 K tracked closely with the experimental data points and showed a noteworthy demonstration with regard to the competency of the new potentials. Where traditional modeling techniques predicted selectivity that was extremely high and fairly unrealistic, the PHAHST force field predicted selectivity in line with the empirical measurements (similar concurrence among results was obtained at 273 K). This result stemmed directly from PHAHST's ability to capture a trend in which the adsorption profiles of krypton and xenon appeared fairly similar, particularly given the ambient conditions, which were highly krypton-rich. Under identical simulated conditions, multiple LJ 12−6 potentials predicted a significant excess in xenon uptake, such that xenon adsorption was predicted to outnumber krypton in the neighborhood of 2 to 1. The fact that the behavior predicted by the PHAHST model was so precisely borne out by the empirical data certainly builds confidence in these models, especially at the state points in which they were performed.

ASSOCIATED CONTENT

Supporting Information

The Supporting Information is available free of charge at https://pubs.acs.org/doi/10.1021/acs.jctc.4c00226.

LaTeX source file (ZIP)

Calculation of Henry's constant for krypton and xenon using PHAHST model and LJ potential; simulation snapshots(PDF)

AUTHOR INFORMATION

Corresponding Authors

Logan Ritter − *Department of Chemistry, North Carolina State University, Raleigh, North Carolina 27695, United States;* orcid.org/0000-0002-2759-4588; Email: lritter@ncsu.edu

Brant Tudor − *John Hopkins School of Medicine, Anesthesiology and Critical Care Medicine, Saint Petersburg, Florida 33701, United States;* Email: btudor4@jh.edu

Brian Space − *Department of Chemistry, North Carolina State University, Raleigh, North Carolina 27695, United States;* orcid.org/0000-0003-0246-7408; Email: bspace@ncsu.edu

Authors

Adam Hogan − *Department of Chemistry, North Carolina State University, Raleigh, North Carolina 27695, United States*

Tony Pham − *Department of Chemistry, University of South Florida, Tampa, Florida 33620, United States;* orcid.org/0000-0001-5654-163X

Complete contact information is available at:

https://doi.org/10.1021/acs.jctc.4c00226
J. Chem. Theory Comput. 2024, 20, 5570−5582

https://pubs.acs.org/10.1021/acs.jctc.4c00226

Author Contributions

L.R. and B.T. contributed equally to this work.

Notes

The authors declare no competing financial interest.

■ ACKNOWLEDGMENTS

L.R., B.T., A.H., T.P., and B.S. acknowledge Bridges-2 at Pittsburgh Supercomputing Center through allocation CHE230105 from the Advanced Cyberinfrastructure Coordination Ecosystem: Services & Support (ACCESS) program, which is supported by the National Science Foundation grants #2138259, #2138286, #2138307, #2137603, and #2138296; the National Science Foundation under grant no. 2154882 to B.S.; the computing resources provided by North Carolina State University High-Performance Computing Services Core Facility (RRID: SCR_022168); and the use of the services provided by Research Computing at the University of South Florida.

■ REFERENCES

(1) Hogan, A.; Space, B. Next-Generation Accurate, Transferable, and Polarizable Potentials for Material Simulations. *J. Chem. Theory Comput.* **2020**, *16*, 7632−7644.
(2) Keyes, T.; Napoleon, R. L. Extending Classical Molecular Theory with Polarization. *J. Phys. Chem. B* **2011**, *115*, 522−531.
(3) Mankoo, P. K.; Keyes, T. POLIR: Polarizable, flexible, transferable water potential optimized for IR spectroscopy. *J. Chem. Phys.* **2008**, *129*, 034504.
(4) Ianovski, D.; Munakata, K.; Kanjo, S.; Yokoyama, Y.; Koga, A.; Yamatsuki, S.; Tanaka, K.; Fukumatsu, T.; Nishikawa, M.; Igarashi, Y. Adsorption of Noble Gases on H-Mordenite. *J. Nucl. Sci. Technol.* **2002**, *39*, 1213−1218.
(5) Banerjee, D.; Simon, C. M.; Plonka, A. M.; Motkuri, R. K.; Liu, J.; Chen, X.; Smit, B.; Parise, J. B.; Haranczyk, M.; Thallapally, P. K. Metal−organic framework with optimally selective xenon adsorption and separation. *Nat. Commun.* **2016**, *7*, ncomms11831.
(6) Banerjee, D.; Cairns, A. J.; Liu, J.; Motkuri, R. K.; Nune, S. K.; Fernandez, C. A.; Krishna, R.; Strachan, D. M.; Thallapally, P. K. Potential of Metal−Organic Frameworks for Separation of Xenon and Krypton. *Acc. Chem. Res.* **2015**, *48*, 211−219.
(7) Niu, Z.; Fan, Z.; Pham, T.; Verma, G.; Forrest, K. A.; Space, B.; Thallapally, P. K.; Al-Enizi, A. M.; Ma, S. Self-Adjusting Metal−Organic Framework for Efficient Capture of Trace Xenon and Krypton. *Angew. Chem., Int. Ed. Engl.* **2022**, *61*, No. e202117807.
(8) Nguyen Sadassivame, J.; Nerisson, P.; Cantrel, L.; Dhainaut, J.; Royer, S.; Loiseau, T.; Volkringer, C. Experimental study on the feasibility for noble gases (Xe, Kr) trapping using Metal-Organic Framework. *ERMSAR2022-The 10th European Review Meeting on Severe Accident Research*; Akademiehotel: Karlsruhe, Germany, 2022.
(9) Soelberg, N. R.; Garn, T. G.; Greenhalgh, M. R.; Law, J. D.; Jubin, R.; Strachan, D. M.; Thallapally, P. K. Radioactive iodine and krypton control for nuclear fuel reprocessing facilities. *Sci. Technol. Nucl. Install.* **2013**, *20131702496*..
(10) Mohamed, M. H.; Elsaidi, S. K.; Pham, T.; Forrest, K. A.; Schaef, H. T.; Hogan, A.; Wojtas, L.; Xu, W.; Space, B.; Zaworotko, M. J.; Thallapally, P. K. Hybrid Ultra-Microporous Materials for Selective Xenon Adsorption and Separation. *Angew. Chem., Int. Ed.* **2016**, *55*, 8285−8289.
(11) Yang, L.; Qian, S.; Wang, X.; Cui, X.; Chen, B.; Xing, H. Energy-efficient separation alternatives: metal−organic frameworks and membranes for hydrocarbon separation. *Chem. Soc. Rev.* **2020**, *49*, 5359−5406.
(12) Lawler, K. V.; Hulvey, Z.; Forster, P. M. Nanoporous metal formates for krypton/xenon separation. *Chem. Commun.* **2013**, *49*, 10959−10961.
(13) Hye Kwon, Y.; Kiang, C.; Benjamin, E.; Crawford, P.; Nair, S.; Bhave, R. Krypton-xenon separation properties of SAPO-34 zeolite materials and membranes. *AIChE J.* **2017**, *63*, 761−769.
(14) Wang, X.; Zhou, T.; Zhang, P.; Yan, W.; Li, Y.; Peng, L.; Veerman, D.; Shi, M.; Gu, X.; Kapteijn, F. High-Silica CHA Zeolite Membrane with Ultra-High Selectivity and Irradiation Stability for Krypton/Xenon Separation. *Angew. Chem., Int. Ed.* **2021**, *60*, 9032−9037.
(15) Akerib, D. S.; Araújo, H.; Bai, X.; Bailey, A.; Balajthy, J.; Beltrame, P.; Bernard, E.; Bernstein, A.; Biesiadzinski, T.; Boulton, E.; et al. Chromatographic separation of radioactive noble gases from xenon. *Astropart. Phys.* **2018**, *97*, 80−87.
(16) Chakraborty, D.; Nandi, S.; Sinnwell, M. A.; Liu, J.; Kushwaha, R.; Thallapally, P. K.; Vaidhyanathan, R. Hyper-Cross-linked Porous Organic Frameworks with Ultramicropores for Selective Xenon Capture. *ACS Appl. Mater. Interfaces* **2019**, *11*, 13279−13284.
(17) Li, J.; Huang, L.; Zou, X.; Zheng, A.; Li, H.; Rong, H.; Zhu, G. Porous organic materials with ultra-small pores and sulfonic functionality for xenon capture with exceptional selectivity. *J. Mater. Chem. A* **2018**, *6*, 11163−11168.
(18) Rowsell, J. L. C.; Yaghi, O. M. Strategies for Hydrogen Storage in Metal−Organic Frameworks. *Angew. Chem., Int. Ed.* **2005**, *44*, 4670−4679.
(19) Li, H.; Wang, K.; Sun, Y.; Lollar, C. T.; Li, J.; Zhou, H.-C. Recent advances in gas storage and separation using metal−organic frameworks. *Mater. Today* **2018**, *21*, 108−121.
(20) García-Holley, P.; Schweitzer, B.; Islamoglu, T.; Liu, Y.; Lin, L.; Rodriguez, S.; Weston, M. H.; Hupp, J. T.; Gómez-Gualdrón, D. A.; Yildirim, T.; Farha, O. K. Benchmark Study of Hydrogen Storage in Metal−Organic Frameworks under Temperature and Pressure Swing Conditions. *ACS Energy Lett.* **2018**, *3*, 748−754.
(21) Bavykina, A.; Kolobov, N.; Khan, I. S.; Bau, J. A.; Ramirez, A.; Gascon, J. Metal−Organic Frameworks in Heterogeneous Catalysis: Recent Progress, New Trends, and Future Perspectives. *Chem. Rev.* **2020**, *120*, 8468−8535.
(22) Yang, D.; Gates, B. C. Catalysis by Metal Organic Frameworks: Perspective and Suggestions for Future Research. *ACS Catal.* **2019**, *9*, 1779−1798.
(23) Li, J.-R.; Kuppler, R. J.; Zhou, H.-C. Selective gas adsorption and separation in metal organic frameworks. *Chem. Soc. Rev.* **2009**, *38*, 1477−1504.
(24) Liu, B.; Yang, Q.; Xue, C.; Zhong, C.; Chen, B.; Smit, B. Enhanced Adsorption Selectivity of Hydrogen/Methane Mixtures in Metal−Organic Frameworks with Interpenetration: A Molecular Simulation Study. *J. Phys. Chem. C* **2008**, *112*, 9854−9860.
(25) Ryan, P.; Farha, O. K.; Broadbelt, L. J.; Snurr, R. Q. Computational screening of metal-organic frameworks for xenon/krypton separation. *AIChE J.* **2011**, *57*, 1759−1766.
(26) Mueller, U.; Schubert, M.; Teich, F.; Puetter, H.; Schierle-Arndt, K.; Pastré, J. Metal−organic frameworks—prospective industrial applications. *J. Mater. Chem.* **2006**, *16*, 626−636.
(27) Idrees, K. B.; Chen, Z.; Zhang, X.; Mian, M. R.; Drout, R. J.; Islamoglu, T.; Farha, O. K. Tailoring Pore Aperture and Structural Defects in Zirconium-Based Metal−Organic Frameworks for Krypton/Xenon Separation. *Chem. Mater.* **2020**, *32*, 3776−3782.
(28) Lee, S.-J.; Kim, S.; Kim, E.-J.; Kim, M.; Bae, Y.-S. Adsorptive separation of xenon/krypton mixtures using ligand controls in a zirconium-based metal-organic framework. *Chem. Eng. J.* **2018**, *335*, 345−351.
(29) Wang, H.; Yao, K.; Zhang, Z.; Jagiello, J.; Gong, Q.; Han, Y.; Li, J. The first example of commensurate adsorption of atomic gas in a MOF and effective separation of xenon from other noble gases. *Chem. Sci.* **2014**, *5*, 620−624.
(30) McDaniel, J. G.; Li, S.; Tylianakis, E.; Snurr, R. Q.; Schmidt, J. R. Evaluation of Force Field Performance for High-Throughput Screening of Gas Uptake in Metal−Organic Frameworks. *J. Phys. Chem. C* **2015**, *119*, 3143−3152.

(31) Erucar, I.; Keskin, S. High-Throughput Molecular Simulations of Metal Organic Frameworks for CO_2 Separation: Opportunities and Challenges. *Front. Mater.* **2018**, *5*, 4.
(32) Vanduyfhuys, L.; Vandenbrande, S.; Verstraelen, T.; Schmid, R.; Waroquier, M.; Van Speybroeck, V. QuickFF: A program for a quick and easy derivation of force fields for metal-organic frameworks from ab initio input. *J. Comput. Chem.* **2015**, *36*, 1015−1027.
(33) Boone, P.; Wilmer, C. E. MOFUN: a Python package for molecular find and replace. *Digital Discovery* **2022**, *1*, 679−688.
(34) Buch, V. Path integral simulations of mixed para-D2 and ortho-D2 clusters: The orientational effects. *J. Chem. Phys.* **1994**, *100*, 7610−7629.
(35) Wang, J.; Wolf, R. M.; Caldwell, J. W.; Kollman, P. A.; Case, D. A. Development and testing of a general amber force field. *J. Comput. Chem.* **2004**, *25*, 1157−1174.
(36) Pearlman, D. A.; Case, D. A.; Caldwell, J. W.; Ross, W. S.; Cheatham, T. E.; DeBolt, S.; Ferguson, D.; Seibel, G.; Kollman, P. AMBER, a package of computer programs for applying molecular mechanics, normal mode analysis, molecular dynamics and free energy calculations to simulate the structural and energetic properties of molecules. *Comput. Phys. Commun.* **1995**, *91*, 1−41.
(37) Potoff, J. J.; Siepmann, J. I. Vapor−liquid equilibria of mixtures containing alkanes, carbon dioxide, and nitrogen. *AIChE J.* **2001**, *47*, 1676−1682.
(38) Jorgensen, W. L.; Maxwell, D. S.; Tirado-Rives, J. Development and Testing of the OPLS All-Atom Force Field on Conformational Energetics and Properties of Organic Liquids. *J. Am. Chem. Soc.* **1996**, *118*, 11225−11236.
(39) Boothroyd, S.; Behara, P. K.; Madin, O.; Hahn, D.; Jang, H.; Gapsys, V.; Wagner, J.; Horton, J.; Dotson, D.; Thompson, M. Development and Benchmarking of Open Force Field 2.0.0 — the Sage Small Molecule Force Field, **2023**, chemrxiv-2022-n2z1c-v2. chemRxiv.
(40) Cioce, C. R.; McLaughlin, K.; Belof, J. L.; Space, B. A polarizable and transferable PHAST N2 potential for use in materials simulation. *J. Chem. Theory Comput.* **2013**, *9*, 5550−5557.
(41) Cisneros, G. A.; Wikfeldt, K. T.; Ojamäe, L.; Lu, J.; Xu, Y.; Torabifard, H.; Bartók, A. P.; Csányi, G.; Molinero, V.; Paesani, F. Modeling Molecular Interactions in Water: From Pairwise to Many-Body Potential Energy Functions. *Chem. Rev.* **2016**, *116*, 7501−7528.
(42) Pham, T.; Forrest, K. A.; Hogan, A.; Tudor, B.; McLaughlin, K.; Belof, J. L.; Eckert, J.; Space, B. Understanding Hydrogen Sorption in In-soc-MOF: A Charged Metal-Organic Framework with Open-Metal Sites, Narrow Channels, and Counterions. *Cryst. Growth Des.* **2015**, *15*, 1460−1471.
(43) Becker, T. M.; Luna-Triguero, A.; Vicent-Luna, J. M.; Lin, L.-C.; Dubbeldam, D.; Calero, S.; Vlugt, T. J. Potential of polarizable force fields for predicting the separation performance of small hydrocarbons in M-MOF-74. *Phys. Chem. Chem. Phys.* **2018**, *20*, 28848−28859.
(44) Ongari, D.; Tiana, D.; Stoneburner, S. J.; Gagliardi, L.; Smit, B. Origin of the Strong Interaction between Polar Molecules and Copper(II) Paddle-Wheels in Metal Organic Frameworks. *J. Phys. Chem. C* **2017**, *121*, 15135−15144.
(45) Peng, X.; Lin, L.-C.; Sun, W.; Smit, B. Water adsorption in metal−organic frameworks with open-metal sites. *AIChE J.* **2015**, *61*, 677−687.
(46) Zang, J.; Nair, S.; Sholl, D. S. Prediction of Water Adsorption in Copper-Based Metal−Organic Frameworks Using Force Fields Derived from Dispersion-Corrected DFT Calculations. *J. Phys. Chem. C* **2013**, *117*, 7519−7525.
(47) Leem, A. Y.; Chen, H. Simulating water adsorption in metal−organic frameworks with open metal sites using the 12−6-4 Lennard−Jones potential. *Mol. Simul.* **2023**, *49*, 1135−1142.
(48) Dzubak, A. L.; Lin, L.-C.; Kim, J.; Swisher, J. A.; Poloni, R.; Maximoff, S. N.; Smit, B.; Gagliardi, L. Ab initio carbon capture in open-site metal−organic frameworks. *Nat. Chem.* **2012**, *4*, 810−816.
(49) Waldman, M.; Hagler, A. New combining rules for rare gas van der waals parameters. *J. Comput. Chem.* **1993**, *14*, 1077−1084.
(50) Nugent, P.; Belmabkhout, Y.; Burd, S. D.; Cairns, A. J.; Luebke, R.; Forrest, K.; Pham, T.; Ma, S.; Space, B.; Wojtas, L.; Eddaoudi, M.; Zaworotko, M. J. Porous materials with optimal adsorption thermodynamics and kinetics for CO2 separation. *Nature* **2013**, *495*, 80−84.
(51) McLaughlin, K.; Cioce, C. R.; Belof, J. L.; Space, B. A molecular H2 potential for heterogeneous simulations including polarization and many-body van der Waals interactions. *J. Chem. Phys.* **2012**, *136*, 194302.
(52) Belof, J. L.; Stern, A. C.; Space, B. An Accurate and Transferable Intermolecular Diatomic Hydrogen Potential for Condensed Phase Simulation. *J. Chem. Theory Comput.* **2008**, *4*, 1332−1337.
(53) Mullen, A. L.; Pham, T.; Forrest, K. A.; Cioce, C. R.; McLaughlin, K.; Space, B. A Polarizable and Transferable PHAST CO2 Potential for Materials Simulation. *J. Chem. Theory Comput.* **2013**, *9*, 5421−5429.
(54) Chui, S. S.-Y.; Lo, S. M.-F.; Charmant, J. P. H.; Orpen, A. G.; Williams, I. D. A Chemically Functionalizable Nanoporous Material $[Cu_3(TMA)_2(H_2O)_3]_n$. *Science* **1999**, *283*, 1148−1150.
(55) Kerry, F. G. *Industrial Gas Handbook: Gas Separation and Purification*; CRC Press: Boca Raton, FL, 2007.
(56) Wilson, A. L.; Popelier, P. L. A. Exponential Relationships Capturing Atomistic Short-Range Repulsion from the Interacting Quantum Atoms (IQA) Method. *J. Phys. Chem. A* **2016**, *120*, 9647−9659.
(57) Rackers, J. A.; Ponder, J. W. Classical Pauli Repulsion: An Anisotropic, Atomic Multipole Model. *J. Chem. Phys.* **2019**, *150*, 084104.
(58) Van Vleet, M. J.; Misquitta, A. J.; Stone, A. J.; Schmidt, J. R. Beyond Born−Mayer: Improved Models for Short-Range Repulsion in ab Initio Force Fields. *J. Chem. Theory Comput.* **2016**, *12*, 3851−3870.
(59) Tang, K.; Toennies, J. P. An improved simple model for the van der Waals potential based on universal damping functions for the dispersion coefficients. *J. Chem. Phys.* **1984**, *80*, 3726−3741.
(60) Thakkar, A. J. Higher dispersion coefficients: Accurate values for hydrogen atoms and simple estimates for other systems. *J. Chem. Phys.* **1988**, *89*, 2092−2098.
(61) Misquitta, A. J.; Stone, A. J. Accurate Induction Energies for Small Organic Molecules: 1. Theory. *J. Chem. Theory Comput.* **2008**, *4*, 7−18.
(62) Aviat, F.; Levitt, A.; Stamm, B.; Maday, Y.; Ren, P.; Ponder, J. W.; Lagardère, L.; Piquemal, J.-P. Truncated Conjugate Gradient: An Optimal Strategy for the Analytical Evaluation of the Many-Body Polarization Energy and Forces in Molecular Simulations. *J. Chem. Theory Comput.* **2017**, *13*, 180−190.
(63) Lagardère, L.; Lipparini, F.; Polack, E.; Stamm, B.; Cancès, É.; Schnieders, M.; Ren, P.; Maday, Y.; Piquemal, J.-P. Scalable Evaluation of Polarization Energy and Associated Forces in Polarizable Molecular Dynamics: II. Toward Massively Parallel Computations Using Smooth Particle Mesh Ewald. *J. Chem. Theory Comput.* **2015**, *11*, 2589−2599.
(64) Pham, T.; Space, B. Insights into the Gas Adsorption Mechanisms in Metal−Organic Frameworks from Classical Molecular Simulations. *Top. Curr. Chem.* **2020**, *378*, 14.
(65) Franz, D. M.; Belof, J. L.; McLaughlin, K.; Cioce, C. R.; Tudor, B.; Hogan, A.; Laratelli, L.; Mulcair, M.; Mostrom, M.; Navas, A.; Stern, A. C.; Forrest, K. A.; Pham, T.; Space, B. MPMC and MCMD: Free High-Performance Simulation Software for Atomistic Systems. *Adv. Theory Simul.* **2019**, *2*, 1900113.
(66) Jones, J. E.; Chapman, S. On the determination of molecular fields. − II. From the equation of state of a gas. *Proc. R. Soc. A* **1924**, *106*, 463−477.
(67) Stone, A. *The Theory of Intermolecular Forces*, 2nd ed.; Oxford University Press: Oxford, UK, 2013.
(68) Kramer, H. L.; Herschbach, D. R. Combination Rules for van der Waals Force Constants. *J. Chem. Phys.* **1970**, *53*, 2792−2800.
(69) Smith, F. T. Atomic Distortion and the Combining Rule for Repulsive Potentials. *Phys. Rev. A: At., Mol., Opt. Phys.* **1972**, *5*, 1708−1713.
(70) McLaughlin, K.; Cioce, C. R.; Pham, T.; Belof, J. L.; Space, B. Efficient calculation of many-body induced electrostatics in molecular systems. *J. Chem. Phys.* **2013**, *139*, 184112.

https://doi.org/10.1021/acs.jctc.4c00226
J. Chem. Theory Comput. 2024, 20, 5570−5582

(71) Thole, B. T. Molecular polarizabilities calculated with a modified dipole interaction. *Chem. Phys.* **1981**, *59*, 341−350.
(72) Applequist, J.; Carl, J. R.; Fung, K.-K. Atom dipole interaction model for molecular polarizability. Application to polyatomic molecules and determination of atom polarizabilities. *J. Am. Chem. Soc.* **1972**, *94*, 2952−2960.
(73) Neese, F. The ORCA program system. *WIREs Comput Mol Sci* **2012**, *2*, 73−78.
(74) Dunning, T. H., Jr. Gaussian basis sets for use in correlated molecular calculations. I. The atoms boron through neon and hydrogen. *J. Chem. Phys.* **1989**, *90*, 1007−1023.
(75) Breneman, C. M.; Wiberg, K. B. Determining atom-centered monopoles from molecular electrostatic potentials. The need for high sampling density in formamide conformational analysis. *J. Comput. Chem.* **1990**, *11*, 361−373.
(76) Sherrill, C. D.; Krylov, A. I.; Byrd, E. F. C.; Head-Gordon, M. Energies and analytic gradients for a coupled-cluster doubles model using variational Brueckner orbitals: Application to symmetry breaking in O4+. *J. Chem. Phys.* **1998**, *109*, 4171−4181.
(77) Jäger, B.; Hellmann, R.; Bich, E.; Vogel, E. State-of-the-art ab initio potential energy curve for the krypton atom pair and thermophysical properties of dilute krypton gas. *J. Chem. Phys.* **2016**, *144*, 114304.
(78) Hellmann, R.; Jäger, B.; Bich, E. State-of-the-art ab initio potential energy curve for the xenon atom pair and related spectroscopic and thermophysical properties. *J. Chem. Phys.* **2017**, *147*, 034304.
(79) Perry, J. J. I.; Teich-McGoldrick, S. L.; Meek, S. T.; Greathouse, J. A.; Haranczyk, M.; Allendorf, M. D. Noble Gas Adsorption in Metal−Organic Frameworks Containing Open Metal Sites. *J. Phys. Chem. C* **2014**, *118*, 11685−11698.
(80) Bae, Y.-S.; Hauser, B. G.; Colón, Y. J.; Hupp, J. T.; Farha, O. K.; Snurr, R. Q. High xenon/krypton selectivity in a metal-organic framework with small pores and strong adsorption sites. *Microporous Mesoporous Mater.* **2013**, *169*, 176−179.
(81) Liu, J.; Thallapally, P. K.; Strachan, D. Metal−Organic Frameworks for Removal of Xe and Kr from Nuclear Fuel Reprocessing Plants. *Langmuir* **2012**, *28*, 11584−11589.
(82) Soleimani Dorcheh, A.; Denysenko, D.; Volkmer, D.; Donner, W.; Hirscher, M. Noble gases and microporous frameworks; from interaction to application. *Microporous Mesoporous Mater.* **2012**, *162*, 64−68.
(83) Murad, S.; Gupta, S. A simple molecular dynamics simulation for calculating Henry's constant and solubility of gases in liquids. *Chem. Phys. Lett.* **2000**, *319*, 60−64.
(84) Sadus, R. J. Molecular Simulation of Henry's Constant at Vapor−Liquid and Liquid−Liquid Phase Boundaries. *J. Phys. Chem. B* **1997**, *101*, 3834−3838.
(85) Nicholson, D.; Parsonage, N. G. *Computer Simulation and the Statistical Mechanics of Adsorption*; Academic Press, 1982.
(86) Dubbeldam, D.; Torres-Knoop, A.; Walton, K. S. On the inner workings of Monte Carlo codes. *Mol. Simul.* **2013**, *39*, 1253−1292.
(87) Karavias, F.; Myers, A. L. Isosteric heats of multicomponent adsorption: thermodynamics and computer simulations. *Langmuir* **1991**, *7*, 3118−3126.
(88) Arora, G.; Sandler, S. I. Air separation by single wall carbon nanotubes: Thermodynamics and adsorptive selectivity. *J. Chem. Phys.* **2005**, *123*, 044705.
(89) Al-Matar, A. K.; Rockstraw, D. A. A generating equation for mixing rules and two new mixing rules for interatomic potential energy parameters. *J. Comput. Chem.* **2004**, *25*, 660−668.
(90) Hudson, G. H.; McCoubrey, J. C. Intermolecular forces between unlike molecules. A more complete form of the combining rules. *Trans. Faraday Soc.* **1960**, *56*, 761−766.
(91) Kühne, T. D.; Iannuzzi, M.; Del Ben, M.; Rybkin, V. V.; Seewald, P.; Stein, F.; Laino, T.; Khaliullin, R. Z.; Schütt, O.; Schiffmann, F.; et al. CP2K: An electronic structure and molecular dynamics software package - Quickstep: Efficient and accurate electronic structure calculations. *J. Chem. Phys.* **2020**, *152*, 194103.
(92) VandeVondele, J.; Krack, M.; Mohamed, F.; Parrinello, M.; Chassaing, T.; Hutter, J. Quickstep: Fast and accurate density functional calculations using a mixed Gaussian and plane waves approach. *Comput. Phys. Commun.* **2005**, *167*, 103−128.
(93) Goedecker, S.; Teter, M.; Hutter, J. Separable dual-space Gaussian pseudopotentials. *Phys. Rev. B: Condens. Matter Mater. Phys.* **1996**, *54*, 1703−1710.
(94) Perdew, J. P.; Burke, K.; Ernzerhof, M. Generalized Gradient Approximation Made Simple. *Phys. Rev. Lett.* **1996**, *77*, 3865−3868.
(95) van Duijneveldt, F. B.; van Duijneveldt-van de Rijdt, J. G. C. M.; van Lenthe, J. H. State of the Art in Counterpoise Theory. *Chem. Rev.* **1994**, *94*, 1873−1885.
(96) Wood, W. W.; Parker, F. R. Monte Carlo Equation of State of Molecules Interacting with the Lennard-Jones Potential. I. A Supercritical Isotherm at about Twice the Critical Temperature. *J. Chem. Phys.* **1957**, *27*, 720−733.

https://doi.org/10.1021/acs.jctc.4c00226
J. Chem. Theory Comput. 2024, 20, 5570−5582